



# A nanoscale p-n junction photoelectrode consisting of an $\text{NiO}_x$ layer on a $\text{TiO}_2/\text{CdS}$ nanorod core-shell structure for highly efficient solar water splitting



Il-han Yoo<sup>a</sup>, Shankara S. Kalanur<sup>b,\*</sup>, Hyungtak Seo<sup>a,b,\*</sup>

<sup>a</sup> Department of Energy Systems Research, Ajou University, Suwon 443-739, Republic of Korea

<sup>b</sup> Department of Materials Science and Engineering, Ajou University, Suwon 443-739, Republic of Korea

## ARTICLE INFO

### Keywords:

$\text{TiO}_2$   
 $\text{CdS}$   
 $\text{NiO}_x$   
 p-n Junction  
 Photoelectrochemical water splitting  
 Band alignment

## ABSTRACT

The  $\text{TiO}_2/\text{CdS}$  system has attracted great attention in solar water-splitting applications owing to its desirable electronic and optical properties. With the aim of enhancing its photoelectrochemical water splitting efficiency, an efficient strategy is proposed via nanostructuring and linking it in a p-n junction configuration with  $\text{NiO}_x$ . The deposition of  $\text{TiO}_2$  nanorods (NRs) and  $\text{CdS}$  was achieved using a hydrothermal synthesis route in the sequence, after which  $\text{NiO}_x$  was deposited via RF magnetron sputtering. Characterisation revealed the uniform deposition of  $\text{CdS}$  onto the  $\text{TiO}_2$  NRs, forming a core-shell morphology, and the deposition of  $\text{NiO}_x$  on top of the  $\text{TiO}_2$ -NR/ $\text{CdS}$  resulted in a nanostructured p-n junction. X-ray photoelectron spectroscopy was used to resolve the valence band edge, and impedance studies confirmed the formation of a p-n junction; accordingly, the probable band edge positions of the photoelectrode were identified. The optimised  $\text{TiO}_2$ -NR/ $\text{CdS}$ - $\text{NiO}_x$  p-n junction electrode exhibited a remarkable photocurrent of  $\sim 30 \text{ mA cm}^{-2}$  (at 1 V vs. Ag/AgCl) under AM 1.5 G simulated sunlight and an incident photon-to-current efficiency of  $\sim 97\%$  at 500 nm. Furthermore, during illumination, the production of  $\text{H}_2$  gas occurred with a faradaic efficiency of 95%. The results of the study demonstrate the advantage of utilizing the  $\text{TiO}_2$ -NR/ $\text{CdS}$ - $\text{NiO}_x$  system in a p-n junction configuration to greatly enhance the charge generation, separation and suppression of the charge recombination, which boosts its photoelectrochemical water-splitting performance.

## 1. Introduction

Hydrogen is recognised as a promising clean energy carrier of the future that could replace depleting fossil fuels and decrease the serious environmental damage associated with them [1]. Moreover, sustainable hydrogen production technology using renewable sources could facilitate its commercial acceptance as a fuel in the future. The photoelectrochemical (PEC) water-splitting process using semiconductors is a promising approach to the carbon-free production of hydrogen and a sustainable solution for the future energy supply [2]. After the successful demonstration of photo-assisted water splitting using  $\text{TiO}_2$  by Fujishima and Honda [3], tremendous effort has been devoted for introducing and investigating various semiconductor materials for efficient PEC water splitting. However, hydrogen production via efficient PEC water splitting remains a scientific challenge.

Among the metal oxide semiconductors,  $\text{TiO}_2$  is the most widely studied material for PEC hydrogen production (via both PEC and

photocatalytic water splitting) owing to its well-matched conduction and valence band (VB) edge potential (with respect to water oxidation and reduction potential), low cost, photo-corrosion resistance and high stability in aqueous conditions [4,5]. Despite these advantages, the PEC activity of  $\text{TiO}_2$  face major limitations due to its wide band gap (3.2 eV), that allows the absorption of only ultraviolet region of incident sunlight and incurs poor conductivity of photo-generated charge carriers, which hampers its reaction rate [6]. Hence, the solar water-splitting efficiency of  $\text{TiO}_2$  tends to decrease when employed as a single-junction photo-anode in a PEC system. Because of its wide band gap,  $\text{TiO}_2$  is generally sensitised with low band gap semiconductors such as dyes,  $\text{CdS}$  etc to extend its light absorption ability [7,8]. In fact,  $\text{TiO}_2$  is the most widely utilized support material for the sensitization of variety of narrow band gap semiconductors in numerous energy related applications including, dye, quantum dot and perovskite solar cell. Importantly, as a support material,  $\text{TiO}_2$  provides an effective pathway for the transport of photogenerated electrons from the sensitizer towards the conducting

\* Corresponding authors at: Department of Materials Science and Engineering, Ajou University, Suwon 443-739, Republic of Korea.

E-mail addresses: [shankarask@ajou.ac.kr](mailto:shankarask@ajou.ac.kr) (S.S. Kalanur), [hseo@ajou.ac.kr](mailto:hseo@ajou.ac.kr) (H. Seo).

substrate for faster and improved charge separation. Furthermore,  $\text{TiO}_2$  can be fabricated in variety of nanostructure thin films having specific advantageous for the efficient PEC water splitting. Most importantly, the 1-D morphology of  $\text{TiO}_2$  is known to provide direct electrical pathways for the photogenerated charges along the nanorod arrays, while providing efficient charge separation across the diameter.

$\text{CdS}$  is one of the most important materials utilised in photo-catalytic applications due to its relatively low work function, high carrier mobility and significant absorption of visible light with a band gap of ~2.3 eV [9,10]. With such advantageous,  $\text{CdS}$  has the potential to act as a key ingredient in PEC system as an efficient light harvesting material to produce high photocurrents and  $\text{H}_2$ . However,  $\text{CdS}$  face limitations such as the rapid recombination of photogenerated electron-hole pairs and photo-corrosion that strongly affects its photocatalytic activity [11,12]. Therefore, resolving the photo-corrosion and increasing the charge separation of  $\text{CdS}$  could allow its effective utilization as a suitable photoanode material in PEC system for efficient  $\text{H}_2$  production. This can be achieved by coating a thin layer of stable material on  $\text{CdS}$  that could avoid the photooxidation of  $\text{CdS}$  by rapid extraction of photogenerated holes and by the refraining from direct contact with the electrolyte. However, like  $\text{TiO}_2$  the solar water-splitting efficiency of  $\text{CdS}$  tends to decrease when used as a single-junction photoanode in the PEC system.

The limitations of both  $\text{TiO}_2$  and  $\text{CdS}$  can be resolved by combining them to form a heterojunction photoelectrode. By the sensitisation of  $\text{CdS}$  on  $\text{TiO}_2$ , the overall optical absorption can be extended to the visible spectrum up to 600 nm (including the UV region) [7]. Furthermore, the  $\text{TiO}_2/\text{CdS}$  heterojunction photoelectrode possesses a higher specific surface area and more active reaction sites compared to individual single-junction electrodes [13]. Importantly, the conduction band (CB) edge of  $\text{CdS}$  is situated more negative than that of  $\text{TiO}_2$ , that allows efficient transfer of the photo-generated electrons from  $\text{CdS}$  to the CB of  $\text{TiO}_2$  during the illumination, whereas the holes remain in the  $\text{CdS}$  VB as a result of the potential gradient at the  $\text{TiO}_2/\text{CdS}$  heterojunction interface [8,13]. This mechanism suppresses the recombination between photo-generated electrons and holes through efficient charge separation and improves the overall photocatalytic activity. Thus, a  $\text{TiO}_2/\text{CdS}$  heterojunction electrode performs significantly more efficient than the individual  $\text{TiO}_2$  and  $\text{CdS}$  photoelectrodes [13,14]. However, the efficiency of  $\text{TiO}_2/\text{CdS}$  heterojunction can be further improved by providing a suitable nanostructure for direct charge transfer and surface coating for efficient charge separation and stability [13,15,16].

In PEC water splitting system, various strategies can be implanted to improve the efficiency of photoelectrodes. For example, the formation of a p-n junction photoelectrode is considered an important strategy to achieve increased electron-hole lifetime, efficient electron-hole separation and the suppression of electron-hole recombination. Because the formation of a p-n junction produces a space-charge region at the electrode junction due to the diffusion of charges [17–19]. The diffusion of electrons and holes towards opposite directions produces an internal electric field at the heterojunction region. During the illumination and with the applied bias potential, the produced internal electrical field in a p-n junction can significantly promote the efficient charge separation and transfer at the interface to produce a high quantum yield [20–23]. Hence, the PEC water-splitting efficiency of n-type photoelectrodes can be increased by combining with a p-type material to form nanostructured p-n junction electrodes. Most importantly, such a coating will ensure the stability against photo-corrosion and control the surface energetics and kinetics.

$\text{NiO}$  is a p-type semiconductor material with a wide band gap of 3.6–4.0 eV and possesses a large work function of 5.0 eV [24]. Recent studies show that  $\text{NiO}$  can be efficiently utilised as a hole transfer layer [25], an interfacial layer in a solar cell [26], a chemically stable coating, a highly active electrocatalyst for the water oxidation [27], a layer to control the surface energetics and kinetics of photoanodes [28]

and as a photocathode [29] in PEC water-splitting devices. Importantly, the effective hole extraction, high hole mobility and stability enables its efficient utilisation as a hole transfer layer and surface coating. Hence, an optimised layer of  $\text{NiO}$  on photoanodes can effectively suppress the charge recombination to achieve efficient charge separation during PEC water splitting [20,27,28,30]. Furthermore, when  $\text{NiO}$  is combined with variety of materials in a heterojunction system, the wide band gap of  $\text{NiO}$  does not restrict/obstruct the light harvesting properties of other narrow band gap semiconductor materials. Hence,  $\text{NiO}$  can also be utilized as surface coating layer for narrow band gap semiconductors for protection against the photo-corrosion. Therefore, inspired by  $\text{NiO}$ 's properties and with the aim of improving the PEC activity in the  $\text{TiO}_2\text{-NR/CdS}$  system, we herein propose a p-n junction photoelectrode that contains n-type  $\text{TiO}_2$  NRs with a  $\text{CdS}$  core-shell structure and p-type  $\text{NiO}_x$ . Moreover, a literature survey revealed that the fabrication and a PEC study of  $\text{TiO}_2\text{-NR/CdS-NiO}_x$  p-n junction photoelectrode has not yet been reported.

Utilizing a hydrothermal method in sequence,  $\text{TiO}_2$  NRs coated with a  $\text{CdS}$  shell structure on a fluorine-doped tin oxide (FTO) substrate was fabricated. A thin layer of  $\text{NiO}_x$  was deposited onto the  $\text{TiO}_2\text{-NR/CdS}$  via RF magnetron sputtering. The  $\text{NiO}_x$ -sputtered condition that produced high PEC activity was chosen as the optimal deposition condition. The characterisation results reveal that  $\text{NiO}_x$  deposition mainly occurred on the top of the  $\text{TiO}_2\text{-NR/CdS}$  shell structure. Compared to the  $\text{TiO}_2\text{-NR/CdS}$  photoanode, the optimised  $\text{TiO}_2\text{-NR/CdS-NiO}_x$  heterojunction photoelectrode exhibited a photocurrent density of ~30 mA cm<sup>-2</sup> (at 1 V vs. Ag/AgCl) under AM 1.5 G illumination. Importantly, an incident photon-to-current efficiency (IPCE) of up to 97% at 500 nm and the hydrogen production with a faradaic efficiency of 95% was achieved using the  $\text{TiO}_2\text{-NR/CdS-NiO}_x$  photoelectrode. The presence of p-n junction in  $\text{TiO}_2\text{-NR/CdS-NiO}_x$  photoelectrode was confirmed via Mott-Schottky and I-V measurements. Furthermore, the band edge positions of  $\text{TiO}_2$ ,  $\text{CdS}$  and  $\text{NiO}_x$  before and after the heterojunction formation were investigated using X-ray photoelectron spectroscopy (XPS) VB edge analysis and electrochemical techniques.

## 2. Experimental

Aligned  $\text{TiO}_2$  nanorods on an FTO substrate were synthesized by employing the previously reported hydrothermal method [31]. In a typical synthesis, 25 mL of HCl (37%, Sigma Aldrich) was mixed with 25 mL of deionised water and stirred for 30 min, after which 0.9 mL of titanium tetra-n-butoxide  $[(\text{CH}_3\text{CH}_2\text{CH}_2\text{CH}_2\text{O})_4\text{Ti}$ , 97.0% Kanto chemical Co., INC, Japan] was added and the mixture was further stirred for 30 min to obtain a transparent synthesis solution. This was then transferred to the Teflon liner of a stainless-steel autoclave, filling 70% of its volume. Previously cleaned FTO substrates ( $2.5 \times 3$  cm) were then placed inside the Teflon liner with the conductive side facing downwards. The hydrothermal synthesis was carried out at 150 °C for 5.5 h in an electric oven, after which the autoclave was allowed to cool down to room temperature. Next, the  $\text{TiO}_2$ -coated FTO substrates were taken out, rinsed thoroughly with deionised water and dried in ambient air. Finally, they were annealed at 450 °C for 2 h for conversion to the crystalline phase (with ramping at 5 °C/min).

The  $\text{CdS}$  core-shell structure on the  $\text{TiO}_2$  NRs was formed by utilizing a previously reported method with slight modifications. Cadmium acetate dihydrate  $[(\text{CH}_3\text{COO})_2\text{Cd} \cdot 2\text{H}_2\text{O}$ , 98%, Daejung chemicals, Korea] was used as a Cd source while thiourea ( $\text{CH}_4\text{N}_2\text{S}$ , 99%, Sigma Aldrich) was used as an S source. The aqueous hydrothermal synthesis solution was obtained by the addition 5 mM of  $(\text{CH}_3\text{COO})_2\text{Cd} \cdot 2\text{H}_2\text{O}$  and 10 mM  $\text{CH}_4\text{N}_2\text{S}$  in 50 mL deionised water. The synthesis solution was transferred to a Teflon-lined stainless-steel autoclave, filling 70% of its volume. The previously synthesised  $\text{TiO}_2$  NR-coated FTO substrates were then placed inside the autoclave the  $\text{TiO}_2$  NRs facing downwards. The hydrothermal synthesis was performed at 120 °C for 1.5 h in an electric oven, after which the autoclave was

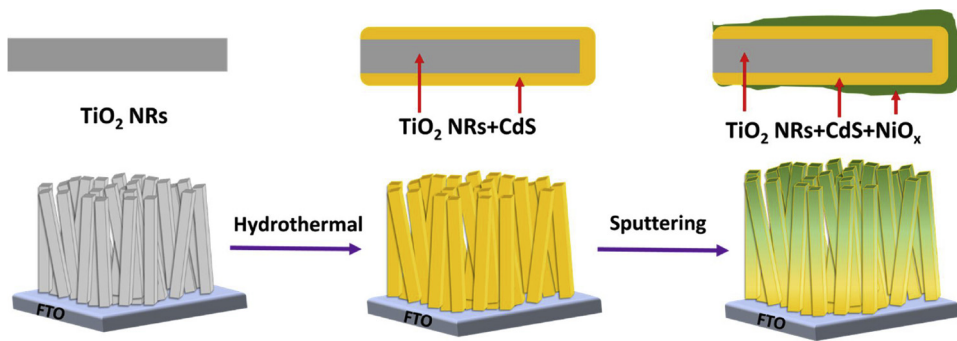


**Fig. 1.** The  $\text{TiO}_2$ -NR/CdS- $\text{NiO}_x$  heterojunction photoelectrode fabrication scheme.

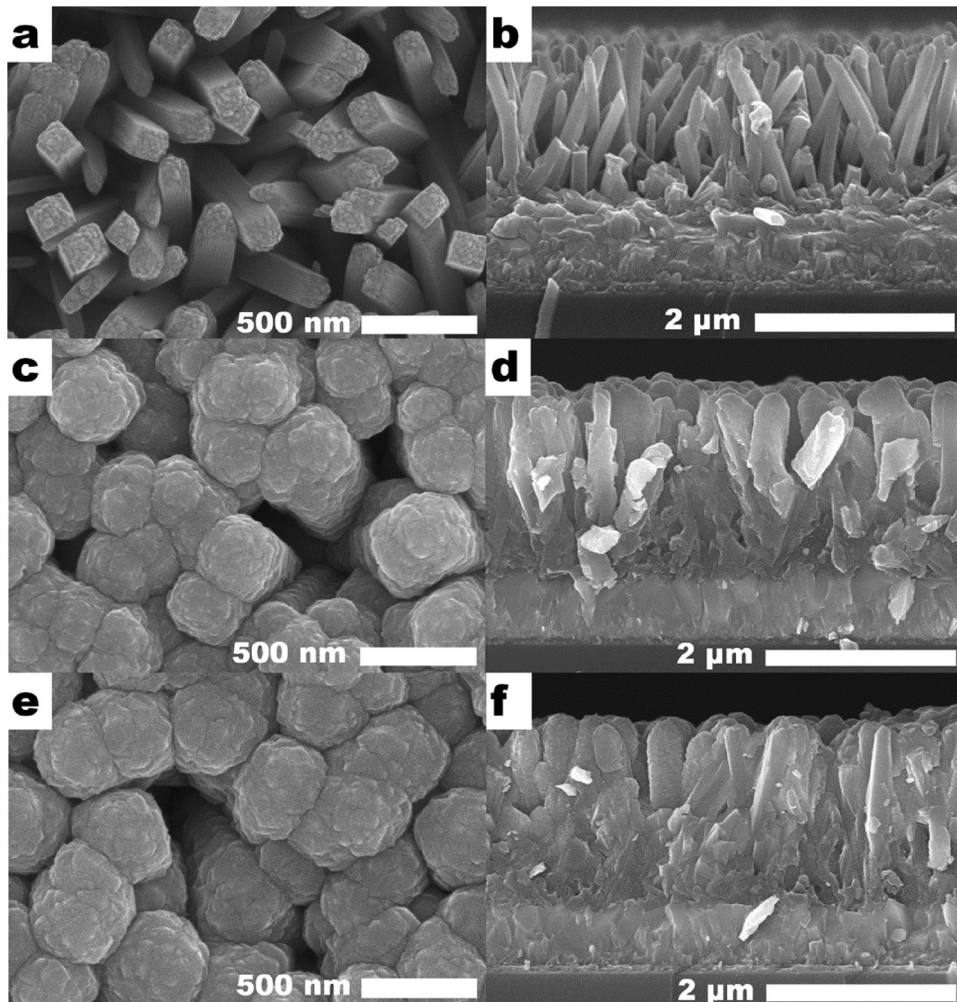


**Fig. 2.** Respective surface and cross-sectional SEM images of the (a and b)  $\text{TiO}_2$  NR, (c and d)  $\text{TiO}_2$ -NR/CdS and (e and f)  $\text{TiO}_2$ -NR/CdS- $\text{NiO}_x$  thin films.

allowed to cool and the CdS-coated  $\text{TiO}_2$  NRs were washed and dried in air. A layer of  $\text{NiO}_x$  on the  $\text{TiO}_2$ /CdS was deposited via RF magnetron sputtering using a metallic Ni target (99.99% purity) in an Ar and  $\text{O}_2$  gas mixture at a ratio of 20:7 (after optimisation). The deposition was carried out for 15 min (after optimisation) with an applied power of 100 W to the target. The substrates were masked with 3 M tape to avoid deposition in unwanted areas. The substrate (FTO- $\text{TiO}_2$ -NR/CdS) was kept in rotation mode at 60 rpm without heating. Note that the optimal condition for  $\text{NiO}_x$  deposition was based on its PEC properties under varied deposition parameters such as gas ratio, flow rate, target power and deposition time. Fig. 1 shows the fabrication scheme for the  $\text{TiO}_2$ -NR/CdS- $\text{NiO}_x$  p-n junction electrode.

The crystalline structures of the  $\text{TiO}_2$ /CdS- $\text{NiO}_x$  thin films were characterised using a MiniFlex (Japan) desktop X-ray diffraction (XRD) instrument with  $\text{Cu K}\alpha$  radiation at a diffraction angle between 10 and 90  $2\theta$ . The surface and cross-sectional morphologies of the  $\text{TiO}_2$ /CdS- $\text{NiO}_x$  thin films were analysed using a JEOL JSM-6700 F (Japan) and a Hitachi S4800 (Japan) scanning electron microscope (SEM). Transmission electron microscope (TEM) measurements were carried out using a JEOL JEM-2100 F (USA) instrument. UV-vis absorption spectra were recorded using a Varian Cary 5000 spectrophotometer (Australia) in integrated sphere scattering mode with a wavelength range of 200–2000 nm. An XPS analysis was carried out with a theta-probe angle-resolved X-ray photoelectron spectrometer (Thermo Fisher

Scientific Co., USA) using a monochromatic micro-focused Al K $\alpha$  (1486.6 eV) source; the peak energy in XPS was self-calibrated to the C 1 s and O 1 s reference peak states. An ABET Technologies Sun 2000 solar simulator (USA) calibrated to AM 1.5 G irradiance conditions was used as the light source. A Thermo Oriel 1000 W xenon arc lamp (Thermo Oriel 66902, USA) combined with a monochromator (Thermo Oriel Cornerstone 7400 1/8) was used to measure the IPCE. The amount of H<sub>2</sub> produced during the PEC activity was quantified using gas chromatography (YOUNG LIN - YL 6500 GC System, Korea) equipped with pulsed discharge ionization detector (PDD) containing capillary column. The gas collected in the sealed reaction cell was pumped into GC using helium carrier gas.

The PEC measurements of the TiO<sub>2</sub>/CdS-NiO<sub>x</sub> thin film photoanode were carried out in a quartz cell with Pt as the counter electrode and Ag/AgCl as the reference electrode in 0.5 M Na<sub>2</sub>S and 0.5 M Na<sub>2</sub>SO<sub>4</sub> electrolyte (separately) with a scan rate of 50 mV s<sup>-1</sup>. The TiO<sub>2</sub>/CdS-NiO<sub>x</sub> photoanodes were masked with an O-ring during the PEC measurement, thereby exposing 0.125 cm<sup>2</sup> of the sample to the incident light source. An electrochemical impedance spectroscopic (EIS) analysis was conducted in the frequency range of 0.1 – 10<sup>5</sup> Hz at 0 V vs. Ag/AgCl using an AC voltage perturbation of 10 mV in a 0.5 M Na<sub>2</sub>S solution. Mott – Schottky measurements were also carried out in the same electrolyte solution in the absence of irradiation. The amount of hydrogen produced during electrolysis was measured using a calibrated pressure sensor. The applied potential was converted to RHE values using the following Nernst equation:

$$E_{\text{RHE}} = E_{\text{Ag/AgCl}} + (0.0591 \times \text{pH}) + E^{\circ}_{\text{Ag/AgCl}}, \quad (1)$$

$$E^{\circ}_{\text{Ag/AgCl}} (3.0 \text{M NaCl}) = 0.209 \text{V at } 25^\circ\text{C}.$$

### 3. Results and discussion

Fig. 2a and b show the top and cross-sectional views of the TiO<sub>2</sub> NRs deposited on the FTO substrate, respectively. The TiO<sub>2</sub> NRs on FTO substrate were in tetragonal shape with square top facets aligned perpendicular to the substrate. The top surface of the TiO<sub>2</sub> NRs appears to contain many step edges, while the side wall appears smooth. The diameter and length of the TiO<sub>2</sub> NRs were found to be ~100 nm and ~1.8  $\mu\text{m}$ , respectively. After the hydrothermal deposition of CdS onto the TiO<sub>2</sub> NRs, significant changes in morphology and dimension were observed. The top and cross-sectional SEM views shown in Fig. 2c and d confirm the complete coverage of CdS on the TiO<sub>2</sub> NRs forming a core-shell structure. After the CdS deposition, the overall dimension of the NRs appeared to have increased to 200–300 nm, whereas the length of the NRs increased to ~2  $\mu\text{m}$ . Furthermore, the space between the NRs appeared to have narrowed due to CdS deposition. After the sputter deposition of NiO<sub>x</sub> onto TiO<sub>2</sub>-NR/CdS, no significant change was noticed in dimension and the length of NRs. Importantly, the sputter deposition conditions did not affect the morphology of TiO<sub>2</sub>-NR/CdS, as evident in Fig. 2e and f. In these images (Fig. 2e and f), the NiO<sub>x</sub> layers deposited on TiO<sub>2</sub>-NR/CdS cannot be seen clearly due to the smaller particle size of NiO<sub>x</sub>. After the magnification of surface SEM images, the change in surface roughness was noticed (Fig. S1) confirming the deposition of NiO<sub>x</sub> nanoparticles on the top of TiO<sub>2</sub>-NR/CdS. To confirm the nature of NiO<sub>x</sub> deposition, it was sputtered onto the bare FTO and characterised. The Fig. S2 shows the surface and cross section SEM image of NiO<sub>x</sub> deposited on the bare FTO substrate confirming the uniform deposition of NiO<sub>x</sub> consisting of nanoparticles forming a thin-layer structure.

XRD patterns of the fabricated electrodes are shown in Fig. 3. All the XRD patterns contained peaks related to tetragonal SnO<sub>2</sub> (JCPDS No. 46-1088; indicated with black dots) that arise from the FTO substrate (green line). The XRD pattern of the synthesised TiO<sub>2</sub> NRs on FTO substrate (black line) was ascribed to the rutile phase of tetragonal TiO<sub>2</sub> (JCPDS No.88-1175) [31]. The appearance of XRD peaks related to

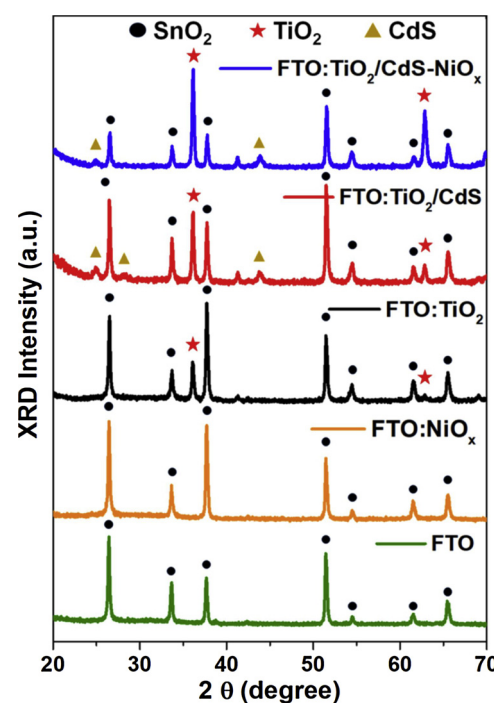


**Fig. 3.** XRD pattern of the FTO substrate and NiO<sub>x</sub>, TiO<sub>2</sub> NR, TiO<sub>2</sub>-NR/CdS and TiO<sub>2</sub>-NR/CdS- NiO<sub>x</sub> thin films on FTO substrates. The black dots indicate the XRD peaks that arise from SnO<sub>2</sub> in the FTO substrate, whereas the XPD peaks indicated by stars and triangles indicate the presence of rutile TiO<sub>2</sub> and hexagonal CdS, respectively.

(101) and (002) planes and the absence of other peaks indicate the preferential growth of TiO<sub>2</sub> NRs and its orientation with respect to the substrate [31]. In the XRD pattern of the TiO<sub>2</sub>-NR/CdS (the red line in Fig. 3), the diffraction peaks arising from CdS can be clearly seen and were assigned to the hexagonal phase of wurtzite CdS (JCPDS card no. 75-1545) [32]. The observed characteristic diffraction peaks at 20 angles of ~24.95, ~26.51, ~28.17 and ~43.80 were respectively assigned to the (100), (002), (101) and (110) planes of the hexagonal CdS phase, respectively. However, the XRD pattern of the FTO-TiO<sub>2</sub>-NR/CdS-NiO<sub>x</sub> (blue line in Fig. 3) and FTO-NiO<sub>x</sub> (orange line in Fig. 3) samples did not show any obvious XRD peaks of the NiO<sub>x</sub> phase, suggesting that the NiO<sub>x</sub> layer was very thin.

TEM was employed for the detailed microscopic characterisation and analysis of the TiO<sub>2</sub>-NR/CdS-NiO<sub>x</sub> junction. The low-resolution TEM image of the TiO<sub>2</sub> NRs shown in Fig. 4a reveals that the TiO<sub>2</sub> NR walls appeared smooth with an NR diameter of ~100 nm. The high-resolution TEM image (Fig. 4b) that shows clear lattice fringes confirms the high crystallinity of the TiO<sub>2</sub> NRs. From these, the interplanar d spacing value was calculated as 0.324 nm assigned to the (110) plane of the rutile TiO<sub>2</sub> phase [31]. The hydrothermal deposition of CdS on the TiO<sub>2</sub> NRs was found to have increased the overall NR diameter to ~275 ± 25 nm with a corresponding change in the surface smoothness (Fig. 4c). The overall increase in the NR diameter indicates that the thickness of CdS was around 75–100 nm. Importantly, the deposition of CdS was uniform throughout the TiO<sub>2</sub> NR surface, thus confirming the formation of a core-shell structure. The interplanar d spacing value of 0.35 nm (Fig. 4d) obtained from the high-resolution TEM image was indexed to the (100) plane of the hexagonal CdS. Furthermore, the high-resolution TEM images in Fig. 4e and f clearly indicate the interface between the TiO<sub>2</sub> and CdS without any barrier, which would be beneficial for better charge transfer at the interface. Hence, it can be concluded that the proposed procedure yielded uniformly distributed and highly crystalline CdS on the TiO<sub>2</sub> NRs. The deposition of NiO<sub>x</sub> onto TiO<sub>2</sub>-NR/CdS showed no significant change in the NR diameter or

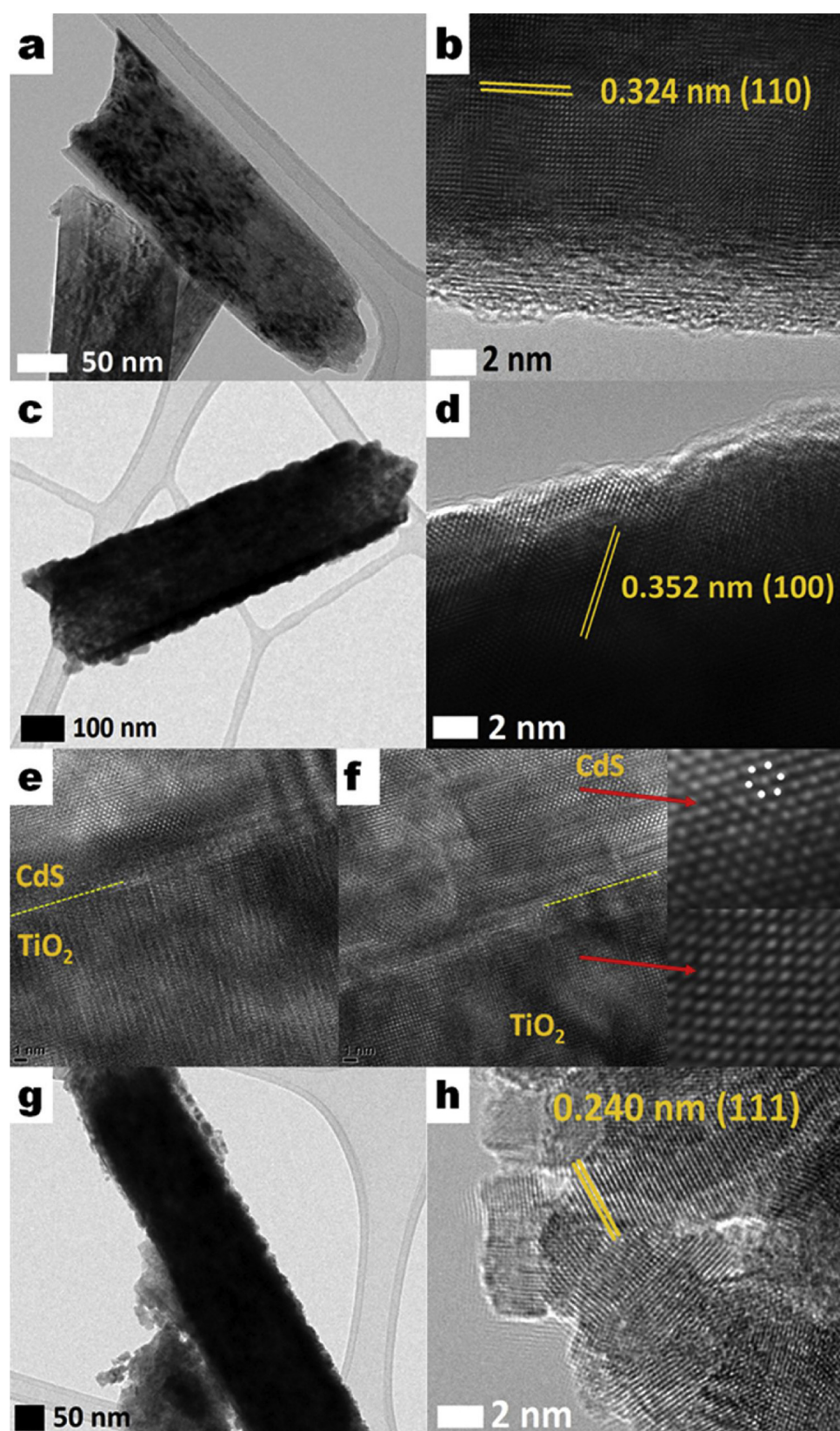


**Fig. 4.** Respective low- and high-resolution TEM images with d-spacing values of the (a and b)  $\text{TiO}_2$  NRs, (c and d)  $\text{TiO}_2$ -NR/CdS and (g and h)  $\text{TiO}_2$ -NR/CdS- $\text{NiO}_x$ ; (e and f) high-resolution TEM images showing the interface between  $\text{TiO}_2$  and CdS.

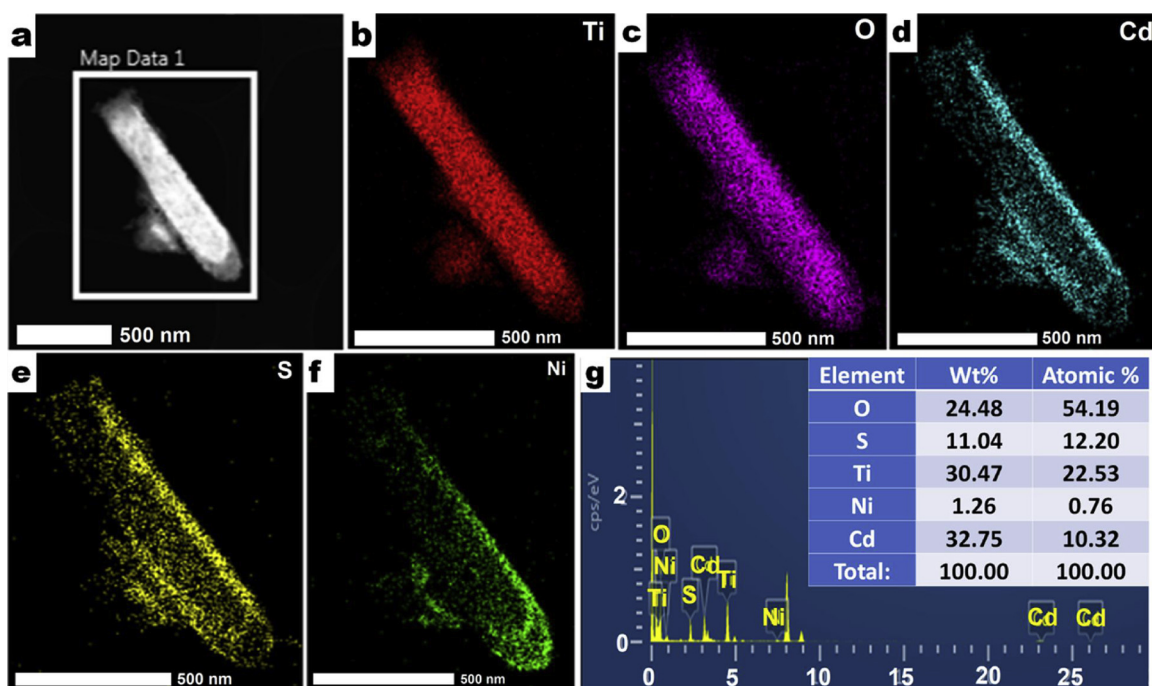


**Fig. 5.** (a) STEM image of  $\text{TiO}_2$ -NR/CdS- $\text{NiO}_x$  showing the selected area for elemental EDS mapping. Elemental mapping images of (b) Ti, (c) O, (d) Cd, (e) S and (f) Ni. (g) EDS spectrum of  $\text{TiO}_2$ -NR/CdS- $\text{NiO}_x$  in the selected area. The inset table shows the elemental analysis data.

surface roughness (Fig. 4g) due to the low amount of deposited  $\text{NiO}_x$ . The TEM analysis at various locations on the NRs revealed that noticeable amounts of  $\text{NiO}_x$  were deposited on the top compared to the surface or bottom of the  $\text{TiO}_2$ -NR/CdS. The interplanar d-spacing value of 0.24 nm was obtained from the lattice fringes (Fig. 4h), which was assigned to the (111) plane of the cubic phase of  $\text{NiO}_x$  [33]. The TEM images shown in Fig. S3 indicate that the particle size of  $\text{NiO}_x$  was between ~2–10 nm (with an average diameter of 5 nm). Due to the uneven deposition of  $\text{NiO}_x$  on the  $\text{TiO}_2$ -NR/CdS, the exact thickness of the  $\text{NiO}_x$  could not be determined using TEM. Furthermore, the interplanar d-spacing value of 0.20 nm observed in Fig. S3d was assigned to the (111) plane of metallic Ni [34], indicating the presence of highly crystalline  $\text{NiO}_x$  having multiple phases.

Energy-dispersive X-ray spectroscopy (EDS) mapping was employed to confirm the distribution and quantity of the individual elements present in  $\text{TiO}_2$ -NR/CdS- $\text{NiO}_x$  (Fig. 5 and S4). The analysis confirmed the presence of Ti, O, Cd, S and Ni without any impurities. The elemental mapping images in the selected area confirmed the uniform deposition of CdS on the  $\text{TiO}_2$  NRs. Note that its thickness was dependent on the deposition time, as shown in Fig. S4. A careful observation of Fig. 5f confirmed that the deposition of  $\text{NiO}_x$  mainly occurred on the top of  $\text{TiO}_2$ -NR/CdS, with a very small amount deposited on the surface. The thickness of the  $\text{NiO}_x$  layer on the top of the  $\text{TiO}_2$ -NR/CdS was ~70–100 nm.

The UV-Vis absorption spectra of the  $\text{TiO}_2$  NRs,  $\text{NiO}_x$ ,  $\text{TiO}_2$ -NR/CdS and  $\text{TiO}_2$ -NR/CdS- $\text{NiO}_x$  are shown in Fig. 6a. The bare  $\text{TiO}_2$  NRs absorb only UV light with wavelengths < 410 nm (red line). Upon the deposition of CdS, the light absorption of  $\text{TiO}_2$  was extended to the visible region up to 550 nm (blue line). However, the deposition of  $\text{NiO}_x$  on  $\text{TiO}_2$ -NR/CdS caused slight red shift in the absorption onset (pink). As is evident (black line), the  $\text{NiO}_x$  thin films ( $\text{NiO}_x$  deposited on FTO) exhibited absorption onset at 350 nm with tailing in the visible region, confirming the presence of oxygen-deficient  $\text{NiO}_x$  and/or metallic Ni. The band gaps of the  $\text{TiO}_2$  NR,  $\text{NiO}_x$ ,  $\text{TiO}_2$ -NR/CdS and  $\text{TiO}_2$ -NR/CdS- $\text{NiO}_x$  photoelectrodes were determined by plotting  $(\alpha h\nu)^2$  as a function of  $h\nu$  as shown in Fig. 6b. In accordance with the absorption onsets, the band gaps of ~3.0, 3.5, 2.26 and 2.25 eV were obtained for the  $\text{TiO}_2$  NR,  $\text{NiO}_x$ ,  $\text{TiO}_2$ -NR/CdS and  $\text{TiO}_2$ -NR/CdS- $\text{NiO}_x$  photoelectrodes,

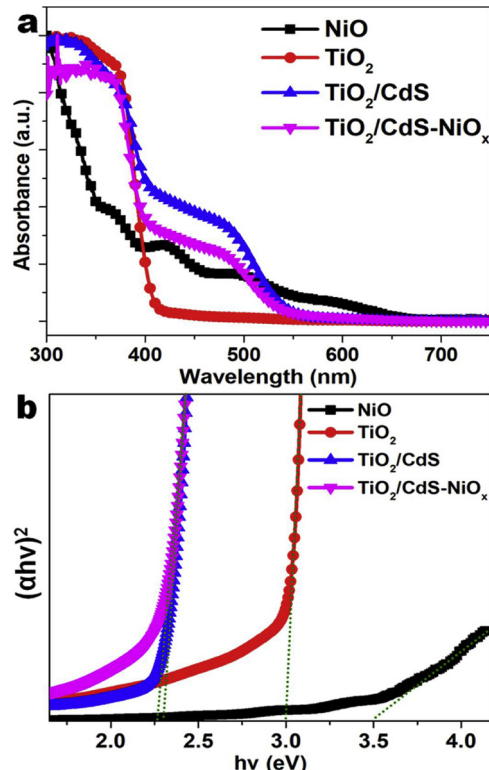


**Fig. 6.** (a) UV-vis absorbance spectra and (b) Tauc plots of NiO,  $\text{TiO}_2$  NR,  $\text{TiO}_2$ -NR/CdS and  $\text{TiO}_2$ -NR/CdS- $\text{NiO}_x$  thin films on FTO substrates yielding band gaps of 3.51, 3.01, 2.30 and 2.26 eV, respectively.

respectively.

XPS was employed to determine the surface electronic state of the elements present in the photoelectrode, as shown in Fig. 7. The high-resolution XPS graph of Ti exhibited two peaks (Fig. 7a) ascribed to the  $\text{Ti} 2p_{3/2}$  and  $\text{Ti} 2p_{1/2}$  at a binding energy values of 458.7 and 464.4 eV,

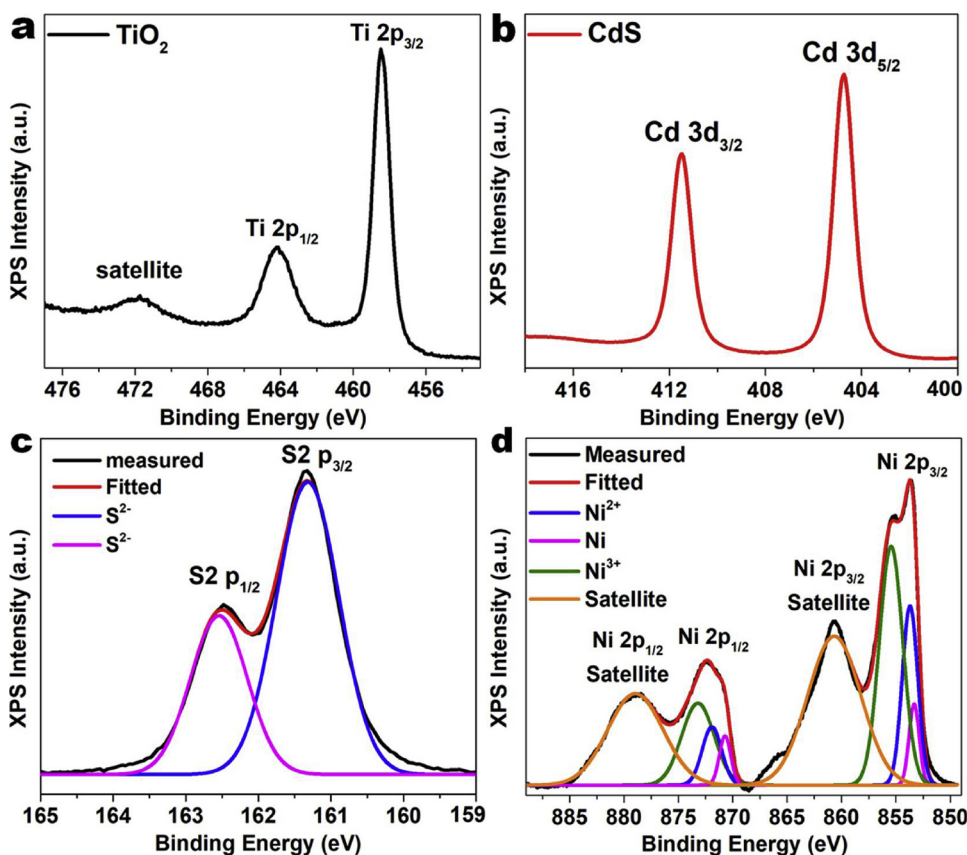


**Fig. 7.** High-resolution XPS spectra of (a) Ti 2p and (b) Cd 3d; deconvoluted high-resolution XPS spectra of (c) S 2p and (d) Ni 2p.

respectively which agree with the typical values of TiO<sub>2</sub> having the Ti<sup>4+</sup> state [35]. Furthermore, the deconvolution of the Ti spectra did not produce any additional peaks, thereby confirming the presence of only the Ti<sup>4+</sup> state in the TiO<sub>2</sub> NR. In addition, a high-energy shake up satellites at ~472.4 eV was noticed, indicating that the free energy of formation of TiO<sub>2</sub> is favoured over other titanium oxides as per the theoretical thermodynamics [36–38]. The high-resolution core level XP spectrum of Cd 3d exhibited two peaks (Fig. 7b) at binding energy values of ~405.00 and ~411.10 eV arising from Cd 3d<sub>3/2</sub> and Cd 3d<sub>5/2</sub>, respectively. This confirms the valency of Cd<sup>2+</sup> in the CdS layer deposited no the TiO<sub>2</sub> NR [39]. Fig. 7c shows the high-resolution deconvoluted XP spectrum of S 2p. The S 2p spectrum exhibited two characteristic peaks arising from S 2p<sub>3/2</sub> and S 2p<sub>1/2</sub> at binding energy values of 161.5 and ~162.7 eV, respectively, which are attributed to the sulphide moiety of CdS. Importantly, the deconvolution did not yield any peaks relevant to the disulphide moiety. The Ni exhibited characteristic XPS peaks arising from Ni 2p<sub>3/2</sub> and Ni 2p<sub>1/2</sub>. Interestingly, the deconvolution of Ni 2p XPS spectrum produced three peaks at 854.7, 856.0 and 852.9 eV (Fig. 7d) that respectively arose from Ni<sup>2+</sup>, Ni<sup>3+</sup> and Ni<sup>0</sup> states [40], confirming the presence of NiO, Ni<sub>2</sub>O<sub>3</sub> and metallic Ni in the TiO<sub>2</sub>-NR/CdS-NiO<sub>x</sub> heterojunction photoelectrode.

The PEC properties of the electrodes were analysed using linear sweeping voltammetry (LSV) under AM 1.5 G simulated solar light irradiation (i.e. 100 mW cm<sup>-2</sup>) with the back-side illumination setup. By considering the stability of CdS, the PEC activities were tested in two different electrolytes: 0.5 M Na<sub>2</sub>S and 0.5 M Na<sub>2</sub>SO<sub>4</sub>. The LSV voltammograms of the TiO<sub>2</sub> NR, TiO<sub>2</sub>-NR/CdS and TiO<sub>2</sub>-NR/CdS-NiO<sub>x</sub> films in the presence and absence of illumination (dark) are shown in Fig. 8a. The TiO<sub>2</sub> NRs, TiO<sub>2</sub>-NR/CdS and TiO<sub>2</sub>-NR/CdS-NiO<sub>x</sub> electrodes exhibited negligible/no photocurrent in the absence of illumination. The photocurrent density of TiO<sub>2</sub> NRs significantly increased after the deposition of CdS. The TiO<sub>2</sub> NRs and optimised TiO<sub>2</sub>-NR/CdS (the CdS deposition time optimisation, see Fig. S5a) electrodes exhibited

respective photocurrent densities of 1.2 and 3.2 mA cm<sup>-2</sup>. After the deposition of NiO<sub>x</sub> on TiO<sub>2</sub>-NR/CdS, a dramatic enhancement in the photocurrent was observed. Here, the amount of NiO<sub>x</sub> deposited on TiO<sub>2</sub>-NR/CdS can be controlled by varying the sputtering deposition time. The photocurrent of TiO<sub>2</sub>-NR/CdS show gradual increase with the increase in deposition time until 15 min. Above the 15 min. of deposition time tends to cause rapid decrease in photocurrent. Therefore, 15 min. of NiO<sub>x</sub> deposition time was selected as optimum deposition condition. For the optimised NiO<sub>x</sub> deposition for TiO<sub>2</sub>-NR/CdS-NiO<sub>x</sub> films (see Fig. S5b), a record photocurrent of ~30 mA cm<sup>-2</sup> was observed. Clearly, the photocurrent obtained for the TiO<sub>2</sub>-NR/CdS-NiO<sub>x</sub> electrode was significantly greater than that for the individual TiO<sub>2</sub> NRs and the TiO<sub>2</sub>-NR/CdS electrodes. Interestingly, the deposition of NiO<sub>x</sub> causes anodic shift in onset potential and comparatively lower photocurrents were observed at low bias voltages (-1.2 to -0.6 V) as noticed in Fig. 8a. It can be speculated that, the anodic shift in flat band potential might be caused by the surface states that effect the charge on the outer surface of the electrode which could lower the conduction band at the surface and hence shift onset potential anodically. Because, the synthesized NiO<sub>x</sub> layer on TiO<sub>2</sub>-NR/CdS consists of multiple phases that could result in a significant amount of surface states. Moreover, a large photocurrent observed at high bias could also be ascribed to the large drive force for the surface reaction (S<sup>2-</sup> to S<sub>2</sub><sup>2-</sup>). Overall, the high photocurrent obtained for the optimised electrodes could have been due to the hole scavenging, charge transport properties of NiO<sub>x</sub> forming p-n junction electrodes for efficient charge separation and migration along with the suppression of the charge recombination [41].

The IPCE values were obtained to study the photo-response of electrodes as a function of the incident light wavelength. Fig. 8b represents the IPCE plot of TiO<sub>2</sub> NRs, TiO<sub>2</sub>-NR/CdS and TiO<sub>2</sub>-NR/CdS-NiO<sub>x</sub> electrodes measured with an applied bias of 0 V vs. Ag/AgCl in 0.5 Na<sub>2</sub>S electrolyte as follows:

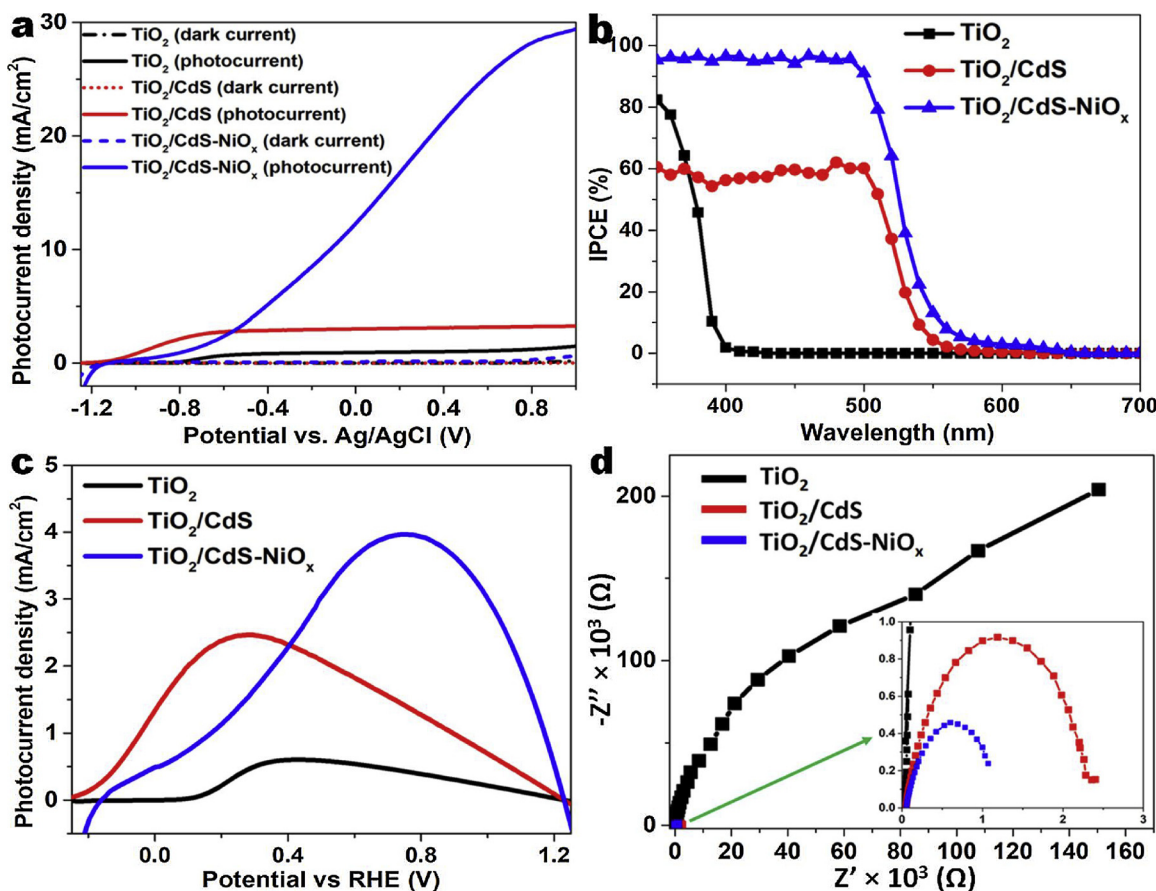


**Fig. 8.** (a) LSVs, (b) IPCEs, (c) photo-conversion efficiencies and (d) Nyquist plots of the TiO<sub>2</sub> NR, TiO<sub>2</sub>-NR/CdS and TiO<sub>2</sub>-NR/CdS-NiO<sub>x</sub> electrodes. IPCE and impedance were measured at an applied bias voltage of 0 V vs. Ag/AgCl in 0.5 M Na<sub>2</sub>S solution. The full lines and the dotted lines in (a) represent the LSV graphs measured under the presence and absence of illumination, respectively for the corresponding photoelectrodes.

$$\text{IPCE} = [(1240 I) / (\lambda J_{\text{light}})] \times 100, \quad (2)$$

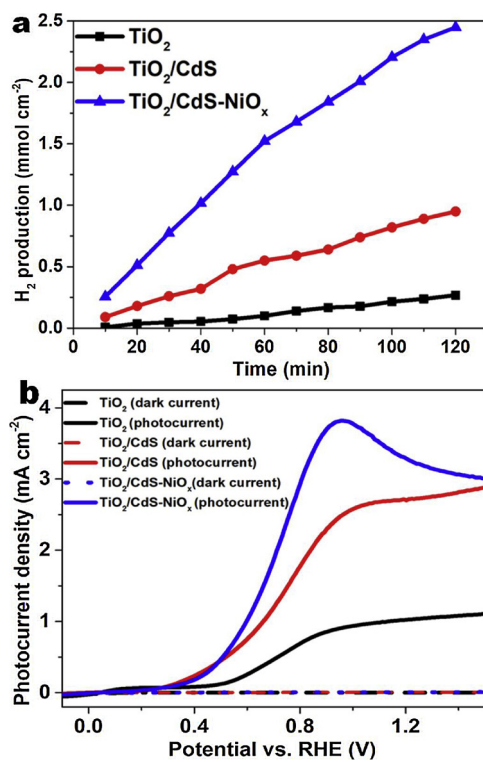
where  $I$  is the photocurrent density,  $\lambda$  is the incident light wavelength and  $J_{\text{light}}$  is the measured irradiance. In accordance with the absorbance results, the TiO<sub>2</sub> NR electrode did not produce IPCE beyond 400 nm. After the deposition of CdS on TiO<sub>2</sub> NR, the IPCE onset showed a significant red shift reaching maximum IPCE values of 60% at 500 nm. The subsequent deposition of NiO<sub>x</sub> caused a dramatic enhancement in IPCE value to ~97% (at 500 nm) with a slight red shift in onset. These observations clearly confirm that the NiO<sub>x</sub> deposition on TiO<sub>2</sub>-NR/CdS electrodes improved the visible-light absorption and enabled efficient charge separation and transportation, thereby producing a record enhancement in IPCE value in the visible spectrum. Fig. S6 shows the IPCE values and their corresponding integration plots for the TiO<sub>2</sub> NR, TiO<sub>2</sub>-NR/CdS and TiO<sub>2</sub>-NR/CdS-NiO<sub>x</sub> electrodes. The integration of the IPCE values in the wavelength range of 300–700 nm produced the expected photocurrent values that appeared at 0 V vs. Ag/AgCl, as shown in Fig. 8a, thus validating the measured photocurrent values under 1 sun illumination. Furthermore, the stabilities of the TiO<sub>2</sub> NR, TiO<sub>2</sub>-NR/CdS and TiO<sub>2</sub>-NR/CdS-NiO<sub>x</sub> electrodes were investigated by measuring the transient currents ( $I-t$ ) with an applied bias of 0 V vs. Ag/AgCl under 1 sun illumination (Fig. S7). All of the electrodes showed a sudden increase in photocurrent value when illuminated after 1 min that stabilised over time. All the electrodes exhibited constant photocurrent values, even after 4 h of illumination, indicating their significant stability over the observed time range.

Fig. 8c represents the photo-conversion (i.e. photon-to-hydrogen) efficiencies of the electrodes calculated using the following equation [42]:

$$\eta (\%) = [I (E_{\text{rev}}^{\circ} - V)] / J_{\text{light}}, \quad (3)$$

where  $\eta$  is the photo-conversion efficiency,  $I$  is the photocurrent density (mA cm<sup>-2</sup>),  $J_{\text{light}}$  is the incident light irradiance (mW cm<sup>-2</sup>),  $E_{\text{rev}}^{\circ}$  is the standard reversible potential (1.23 V vs. RHE) and  $V$  is the applied bias potential vs. RHE. The TiO<sub>2</sub>-NR electrode exhibited the lowest photo-conversion efficiency of 0.72% at 0.41 V vs. RHE, while the TiO<sub>2</sub>-NR/CdS photoanode showed the efficiency of 2.5% at 0.30 V vs. RHE. Importantly, the deposition of NiO<sub>x</sub> on TiO<sub>2</sub>-NR/CdS photoanode increased the photo-conversion efficiency to 4% at 0.78 V vs. RHE along with a positive shift in potential. Here, the observed positive shift in potential confirm the alteration in the electronic structures of TiO<sub>2</sub> NRs in TiO<sub>2</sub>-NR/CdS by the subsequent deposition of CdS and NiO<sub>x</sub>, respectively [43]. Electrochemical impedance spectra (EIS) were acquired to evaluate the charge-transfer resistance across the electrode-electrolyte interface. The corresponding Nyquist plots of TiO<sub>2</sub> NRs, TiO<sub>2</sub>-NR/CdS and TiO<sub>2</sub>-NR/CdS-NiO<sub>x</sub> measured under illumination are presented in Fig. 8d. Compared to the TiO<sub>2</sub> NRs and the TiO<sub>2</sub>-NR/CdS electrode, TiO<sub>2</sub>-NR/CdS-NiO<sub>x</sub> exhibited a smaller semicircle indicating that the deposition of NiO<sub>x</sub> on TiO<sub>2</sub>-NR/CdS yielded lower charge transfer resistance across the electrode-electrolyte interface and thus better charge transfer across the interface, which could have enhanced the PEC activity.

The TiO<sub>2</sub>-NR/CdS-NiO<sub>x</sub> p-n junction electrodes were tested for hydrogen evolution under simulated AM 1.5 G solar illumination in 0.5 M Na<sub>2</sub>S electrolyte. Fig. 9a shows the H<sub>2</sub> gas production rates of the TiO<sub>2</sub>-NR, TiO<sub>2</sub>-NR/CdS and TiO<sub>2</sub>-NR/CdS-NiO<sub>x</sub> photoelectrodes measured during 2 h of continuous irradiation. Compared to TiO<sub>2</sub>-NR, the TiO<sub>2</sub>-NR/CdS show significantly higher hydrogen production rate due to the extended light absorption. Importantly, the rate of H<sub>2</sub> production



**Fig. 9.** (a) The production of hydrogen at the  $TiO_2$ -NR/CdS- $NiO_x$  electrode (at 0 V vs. Ag/AgCl) under AM 1.5 irradiation in a 0.5 M  $Na_2S$  electrolyte. (b) LSVs of the  $TiO_2$  NR,  $TiO_2$ -NR/CdS and  $TiO_2$ -NR/CdS- $NiO_x$  electrodes measured in 0.5 M  $Na_2SO_4$  under 1 sun illumination. The full lines and the dotted lines in (b) show the LSV graphs measured under illumination and dark condition, respectively for corresponding photoelectrodes.

increased dramatically after  $NiO_x$  deposition since the evolution of  $H_2$  for  $TiO_2$ -NR/CdS and  $TiO_2$ -NR/CdS- $NiO_x$  photoelectrodes were measured as 0.5 and 1.3  $mmol\ h^{-1}\ cm^{-2}$ , respectively. The obtained  $H_2$  gas volumes and corresponding I-t curves were used to calculate the faradaic efficiencies of the  $TiO_2$ -NR/CdS and  $TiO_2$ -NR/CdS- $NiO_x$  photoelectrode using the following equation:

$$\text{Faradaic efficiency} = n_{H_2}/(Q/2F), \quad (4)$$

where  $n_{H_2}$  is the total amount of hydrogen produced (mol), Q is the total amount of charge (C) and F is the Faraday constant. During the initial 1 h of hydrogen generation, the faradaic efficiencies of the  $TiO_2$ -NR/CdS and  $TiO_2$ -NR/CdS- $NiO_x$  electrodes were calculated as 80 and 95%, respectively. However, after 2 h of irradiation, the faradaic efficiencies had noticeably decreased to 70 and 90%, respectively. Fig. 9b shows the LS voltammograms of the electrodes measured in 0.5 M  $Na_2SO_4$  electrolyte. 0.5 M  $Na_2S$  acted as a sacrificial electron donor electrolyte via the oxidation of the sulphate moiety and protected the CdS from photo-corrosion, whereas 0.5 M  $Na_2SO_4$  did not contain any sacrificial electron donors, and low comparative photocurrents were thus observed. Importantly, in the case of the 0.5 M  $Na_2SO_4$  electrolyte, a significant increase in the photocurrent was observed after the  $NiO_x$  deposition on  $TiO_2$ -NR/CdS electrodes, indicating the advantages of the  $NiO_x$  layer on the CdS-based electrodes.

A detailed characterization of  $TiO_2$ -NR/CdS- $NiO_x$  electrode was performed after the PEC activity, to investigate its stability after the prolonged irradiation and  $H_2$  production. The SEM images shown in Fig. S8 indicate that no significant change in the morphology was noticed after the PEC measurements. Fig. S9 shows the TEM characterization data of  $TiO_2$ -NR/CdS- $NiO_x$  electrode obtained after the PEC performance. The interplanar d spacing values of 0.321 and 0.359 nm observed in Fig. S9a were assigned to the (110) plane of the rutile  $TiO_2$

and (100) plane of the hexagonal CdS phase, respectively. The interface between the  $TiO_2$  and CdS was clearly seen in Fig. S9b without any barrier. The HR-TEM images shown in Fig. S9c confirm the particle sizes of  $NiO_x$  deposited on the top of  $TiO_2$ -NR/CdS- $NiO_x$  electrode after PEC performance. The interplanar d-spacing value of 0.239 nm and 0.200 nm observed in the Fig. S9d were ascribed (111) plane of the cubic and metallic  $NiO_x$  phase, respectively. Importantly, the TEM characterization indicate that the morphological and crystallographic properties of the  $TiO_2$ -NR/CdS- $NiO_x$  electrode remained stable and unchanged after the PEC performance. Furthermore, the elemental mapping and EDS was used to analyse the distribution and quantity of the individual elements in  $TiO_2$ -NR/CdS- $NiO_x$  electrode after the PEC activity. From Fig. S10, the distribution of all the elements and their quantity was found to be similar to that of  $TiO_2$ -NR/CdS- $NiO_x$  electrode before PEC activity as shown in Fig. 5. The high-resolution core level XP spectrum of Cd 3d, S 2p and Ni 2p measured from the  $TiO_2$ -NR/CdS- $NiO_x$  electrode after the PEC activity are shown in Fig. S11. The XPS spectrum of Cd exhibited two peaks arising from Cd 3d<sub>3/2</sub> and Cd 3d<sub>5/2</sub> confirming the presence of Cd in (II) state. The deconvoluted XPS spectrum of S 2p show two characteristic peaks arising from S 2p<sub>3/2</sub> and S 2p<sub>1/2</sub> ascribed to the sulphide moiety of CdS. The absence of disulfide peak indicates that the CdS is stable under the PEC conditions. The deconvolution of Ni 2p<sub>3/2</sub> and Ni 2p<sub>1/2</sub> yielded three peaks corresponding to Ni<sup>2+</sup>, Ni<sup>3+</sup> and Ni<sup>0</sup> states indicating the presence of NiO, Ni<sub>2</sub>O<sub>3</sub> and metallic Ni. Importantly, the peak ratio of Ni<sup>2+</sup>, Ni<sup>3+</sup> and Ni<sup>0</sup> states were found to be approximately equal to those peaks measured for  $TiO_2$ -NR/CdS- $NiO_x$  electrode before the PEC activity. Overall, the characterization results of  $TiO_2$ -NR/CdS- $NiO_x$  electrode after the PEC activity indicate that the morphology, crystallographic properties, chemical composition and valency of elements remained unchanged confirming the stability of the proposed p-n junction electrode.

A Mott-Schottky (MS) analysis was utilized to identify the electronic characteristics and flat band potentials of the electrodes. The MS plots were measured at the frequency of 0.5 kHz under the absence of illumination using the following equation:

$$1/C^2 = [2/(N_D e \epsilon_0 \epsilon)] [(V_S - V_{fb}) - (k_B T/e)], \quad (5)$$

where C is the space-charge capacitance,  $V_S$  is the applied potential,  $N_D$  is the electron carrier density,  $\epsilon_0$  is the permittivity of the vacuum,  $\epsilon$  is the relative permittivity of the semiconductor, e is the elementary charge, T is the temperature (298 K) and  $k_B$  is the Boltzmann constant. The plot of  $1/C^2$  vs. the applied potential is shown in Fig. 10a-d. Both the  $TiO_2$ -NR (Fig. 10a) and  $TiO_2$ -NR/CdS (Fig. 10b) electrodes exhibited a positive slope, which indicates an n-type semiconductor with electrons as majority carriers. As expected, the MS plots of  $NiO_x$  (Fig. 10c) show a negative slope, thereby confirming a p-type semiconductor. Interestingly, the MS plots of the  $TiO_2$ -NR/CdS- $NiO_x$  electrode showed inverted V shaped curve containing both positive and negative slopes (Fig. 10d), which confirmed the formation of a p-n junction [44]. Importantly, the appearance of both negative and positive slopes indicates that the both the n- and p-type materials are in contact with the electrolyte. This could be due to the uneven deposition of  $NiO_x$  on the  $TiO_2$ -NR/CdS structure. As seen in Fig. 5, the deposition of  $NiO_x$  was noticed to be more on the top of the  $TiO_2$ -NR/CdS structure compared to its side walls. The crossing point of positive and negative slopes shown in Fig. 10d indicate the capacitance values of the space-charge regions of the junction [45]. Furthermore, Fig. 10d shows the MS plots of  $TiO_2$ -NR/CdS- $NiO_x$  p-n junction electrode at different frequencies. From the figure it can be revealed that the capacitance values are dependent on the frequency and the linearity in the graphs indicate the formation of barrier between  $TiO_2$ -NR/CdS- $NiO_x$  p-n junction [46]. Further, the evidence of p-n junction formation was obtained by measuring the I-V characteristics of  $TiO_2$ -NR/CdS- $NiO_x$  electrode in both forward and reverse bias. The I-V characteristics shown in Fig. 10e produce rectification as in the p-n junction diode confirming the

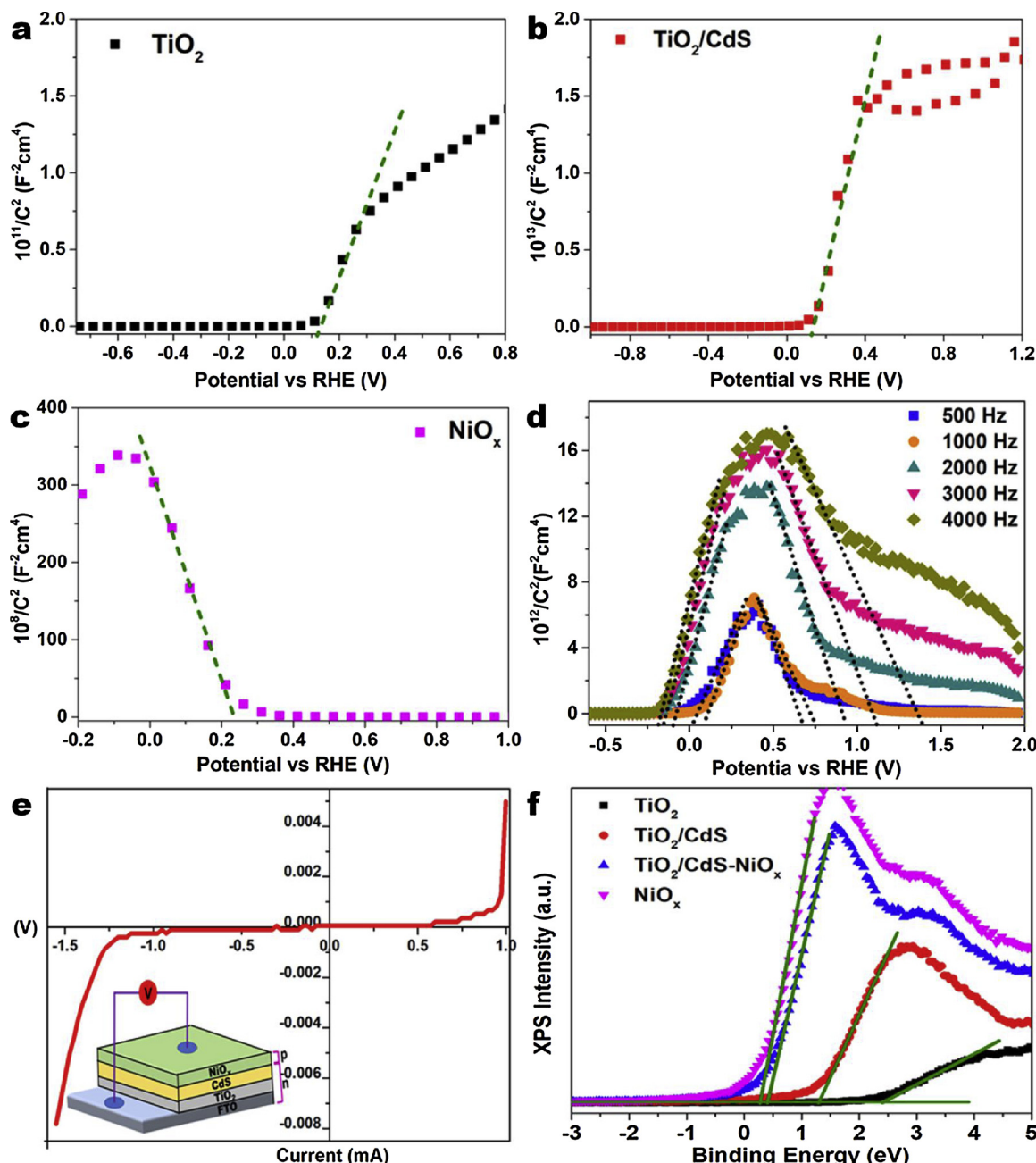


**Fig. 10.** (a) Mott-Schottky plots of (a)  $\text{TiO}_2$ , (b)  $\text{TiO}_2\text{-NR/CdS}$ , (c)  $\text{NiO}_x$ , and (d) the  $\text{TiO}_2\text{-NR/CdS-NiO}_x$  p-n junction electrode. (e) Mott-Schottky plots of  $\text{TiO}_2\text{-NR/CdS-NiO}_x$  p-n junction electrode measured at different frequencies. (e) I-V plots of  $\text{TiO}_2\text{-NR/CdS-NiO}_x$  electrode showing typical characteristic of p-n junction. (f) XPS VB spectra of the  $\text{TiO}_2$ ,  $\text{TiO}_2\text{-NR/CdS}$ ,  $\text{TiO}_2\text{-NR/CdS-NiO}_x$  and  $\text{NiO}_x$  thin films.

formation of  $\text{TiO}_2\text{-NR/CdS-NiO}_x$  p-n junction. It can be noted that, when the polarity of bias voltage is altered, the rectification shows an asymmetrical current flow. In the forward bias region, a sudden increase in the current takes place at the “knee” point whereas, during reverse bias sudden rise in current was noticed at the breakdown voltage. Fig. 10f presents the XPS VB edge graphs of  $\text{NiO}_x$ ,  $\text{TiO}_2$ -NRs,  $\text{TiO}_2\text{-NR/CdS}$  and  $\text{TiO}_2\text{-NR/CdS-NiO}_x$  electrodes. The plots show the energy difference between the Fermi level and the VB edge, thereby confirming the type of electrode. That is, the energy differences for  $\text{TiO}_2$  and  $\text{TiO}_2\text{-NR/CdS}$  was found to be 2.43 and 1.31 eV, respectively, confirming the n-type electrodes, while that of  $\text{NiO}_x$  was 0.26 eV, indicating its p-type characteristics. However, that of the  $\text{TiO}_2\text{-NR/CdS-NiO}_x$  electrode was 0.41 eV, which was mainly due to the  $\text{NiO}_x$  present on the top of the  $\text{TiO}_2\text{-NR/CdS}$  electrode shifting the energy value after the p-n junction formation.

Based on the spectroscopic and electrochemical data, a probable band edge diagram is proposed for the FTO/ $\text{TiO}_2$ , FTO/ $\text{NiO}_x$ , FTO/ $\text{TiO}_2\text{/CdS}$  and  $\text{TiO}_2\text{-NR/CdS-NiO}_x$  electrode as shown in Fig. 11. Depending on the semiconductor, it can be estimated that the flat-band potential ( $E_{fb}$ ) should lie close to the VB or CB. Hence, the CB (the  $\text{TiO}_2$  NR and  $\text{TiO}_2\text{-NR/CdS}$ ) and VB ( $\text{NiO}_x$ ) edge positions of all the electrodes were estimated by determining the  $E_{fb}$  from the intercepts in the MS plots. As can be seen in Fig. 10a, b and c the  $E_{fb}$  of the  $\text{TiO}_2$  NRs,  $\text{TiO}_2\text{-NR/CdS}$  and  $\text{NiO}_x$  were calculated as 0.116, 0.118 and 0.25 V, respectively. Therefore, the CB edge of  $\text{TiO}_2$  and  $\text{TiO}_2\text{/CdS}$  is expected to lie above the  $E_{fb}$  having a potential difference of ~0.1 eV whereas, the VB edge of  $\text{NiO}_x$  is expected to be located at ~0.1 eV below the  $E_{fb}$ . By combining the XPS VB edge and bang gap values, the band edge positions of FTO/ $\text{TiO}_2$ , FTO/ $\text{NiO}_x$ , FTO/ $\text{TiO}_2\text{/CdS}$  were estimated and plotted as shown in Fig. 11a, b and c, respectively. When n-type  $\text{TiO}_2$ ,

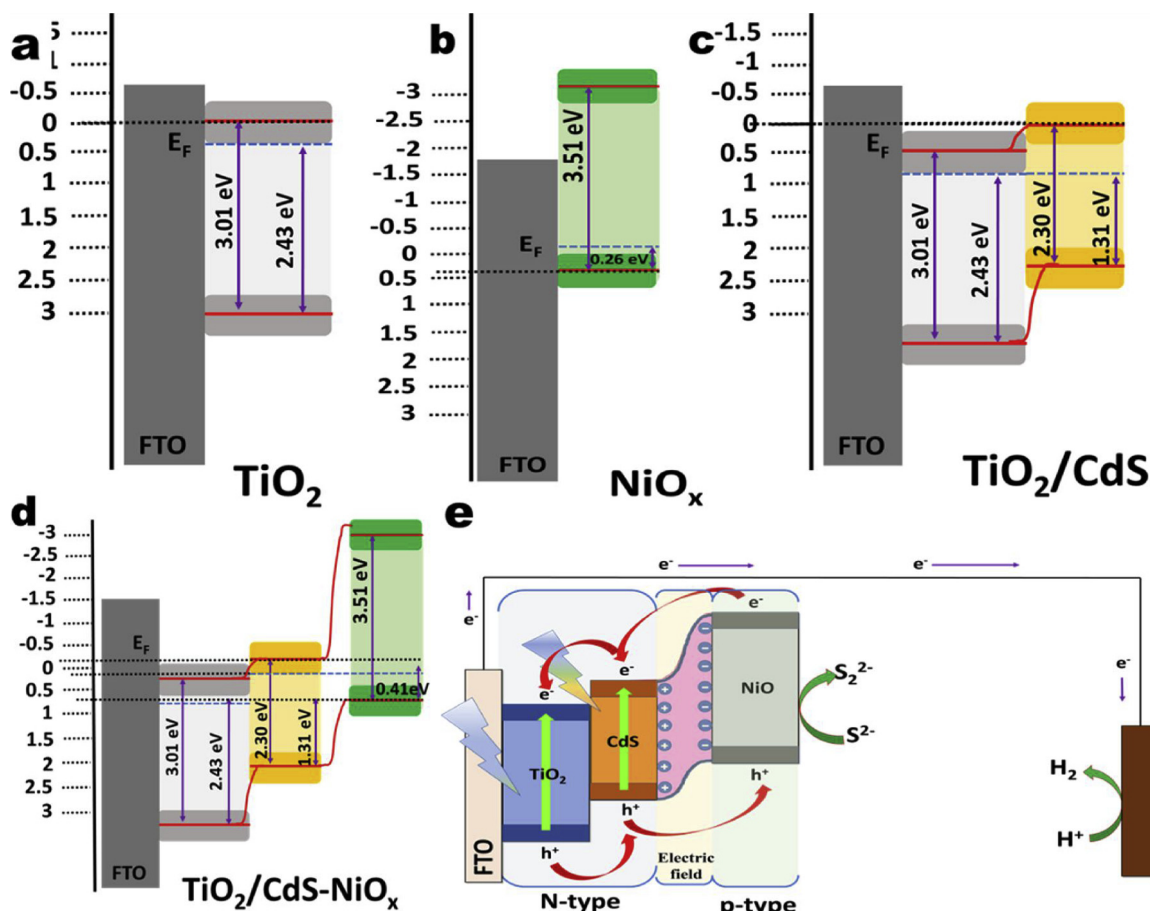


**Fig. 11.** Band-edge alignment of (a)TiO<sub>2</sub>, (b) NiO<sub>x</sub>, (c) TiO<sub>2</sub>-NR/CdS, and (d) the TiO<sub>2</sub>-NR/CdS-NiO<sub>x</sub> p-n junction electrode indicating the VB, CB and Fermi level positions. (e) Schematic diagrams of the p-n junction formation and the PEC water splitting.

NR/CdS and p-type NiO<sub>x</sub> were in contact with each other to form a p-n junction, band bending would have occurred at the interface to reach an equal Fermi level, thereby causing an upward shift in the band-edge position of TiO<sub>2</sub>-NR/CdS and the downward shift of NiO<sub>x</sub>, as is evident in Fig. 11d. That is, the intercept of the positive slope observed at 0.767 V shows the typical characteristics of the VB edge of p-type NiO<sub>x</sub> on the surface whereas the negative slope intercepted at 0.019 V shows the CB edge of the n-type TiO<sub>2</sub>/CdS heterojunction [47]. This suggests that when n-type TiO<sub>2</sub>-NR/CdS is combined with p-type NiO<sub>x</sub>, the band edge positions of the individual materials changed significantly due to band bending and Fermi level alignment, which caused a change in the electron transfer pathway [48]. After the TiO<sub>2</sub>-NR/CdS-NiO<sub>x</sub> p-n junction formation, the electrons near the interface diffused towards the NiO<sub>x</sub> region, which left behind positively charged ions in the TiO<sub>2</sub>-NR/CdS region. Furthermore, the holes near the TiO<sub>2</sub>-NR/CdS-NiO<sub>x</sub> p-n junction interface began to diffuse into the TiO<sub>2</sub>-NR/CdS, thereby leaving ions with a negative charge that led to the formation of a space-charge region at the TiO<sub>2</sub>-NR/CdS-NiO<sub>x</sub> interface. This created an electric field that was able to force photogenerated electrons and holes to transfer in the opposite direction (Fig. 11e). Therefore, the photogenerated electrons and holes in TiO<sub>2</sub>-NR/CdS-NiO<sub>x</sub> were spatially isolated, which led to efficient charge separation. Hence, during the applied bias potential, either an increase or decrease of the band bending could be expected. During anodic polarization, the capacitance of the depletion layer (at the junction) will be minimum favouring the efficient flow of charges. While during the cathodic polarization the capacitance at the junction increases rapidly obstructing the flow of charges [49]. Overall, the characterization results indicate that the enhancement in the PEC properties of TiO<sub>2</sub>-NR/CdS-NiO<sub>x</sub> electrode

could be ascribed to the formation of p-n junction which efficiently separates the photogenerated charges through p-n junction. Additionally, the improved PEC activity was also due to the large drive force for the surface reaction favoured by NiO<sub>x</sub> and the low charge transfer resistances across the electrode/electrolyte interface.

#### 4. Conclusion

We successfully fabricated a nanostructured p-n junction electrode consisting of a NiO<sub>x</sub> layer on a TiO<sub>2</sub> NR and CdS core-shell structure for efficient photoelectrochemical hydrogen generation. Aligned TiO<sub>2</sub> NRs on FTO and the CdS shell structure on the TiO<sub>2</sub> NRs were synthesised using a hydrothermal method in sequence, and a thin layer of NiO<sub>x</sub> was deposited on the top of the TiO<sub>2</sub>-NR/CdS core-shell structure via RF magnetron sputtering. Characterisation confirmed the formation of the highly crystalline tetragonal, hexagonal and cubic phases of TiO<sub>2</sub>, CdS and NiO<sub>x</sub>, respectively. An XPS analysis revealed the presence of NiO<sub>x</sub> with various chemical and electronic states, including Ni<sup>2+</sup>, Ni<sup>3+</sup> and metallic Ni. An XPS VB edge analysis combined with MS plots confirmed the formation of a TiO<sub>2</sub>-NR/CdS-NiO<sub>x</sub> p-n junction electrode. The TiO<sub>2</sub>-NR/CdS-NiO<sub>x</sub> electrode exhibited a record photocurrent of ~30 mA cm<sup>-2</sup> (1 V vs. Ag/AgCl) under full solar spectrum irradiation and an IPCE value of 97% at 500 nm. Furthermore, a superior H<sub>2</sub>-production rate of ~1.3 mmol h<sup>-1</sup> under 1 sun illumination with a faradaic efficiency of 95% was recorded. Based on the electrochemical and spectroscopic data, a change in band edge position before and after the p-n junction formation is proposed. The formation of the TiO<sub>2</sub>-NR/CdS-NiO<sub>x</sub> p-n junction facilitated efficient charge separation and diffusion along with the suppression of electron-hole recombination leading to

enhanced PEC hydrogen production activity. The results of the present work demonstrate an efficient strategy for enhancing the PEC water-splitting activity at the TiO<sub>2</sub>-NR/CdS heterojunction by creating a p–n junction using an NiO<sub>x</sub> layer.

## Acknowledgements

This work was supported by the Technology Development program [C0566106] of the Ministry of SMEs and Startups and the basic Research & Development program [NRF-2017R1D1A1B03035201 and NRF-2019R1A2C2003804] of the Ministry of Science and ICT, Republic of Korea. This work was also supported by Ajou University.

## Appendix A. Supplementary data

Supplementary material related to this article can be found, in the online version, at doi:<https://doi.org/10.1016/j.apcatb.2019.02.063>.

## References

- [1] Hydrogen on the rise, *Nat. Energy.* 1 (2016) 16127, <https://doi.org/10.1038/nenergy.2016.127>.
- [2] E.L. Miller, Photoelectrochemical water splitting, *Energy Environ. Sci.* 8 (2015) 2809–2810, <https://doi.org/10.1039/C5EE90047F>.
- [3] A. Fujishima, K. Honda, Electrochemical photolysis of water at a semiconductor electrode, *Nature* 238 (1972) 238037a0, <https://doi.org/10.1038/238037a0>.
- [4] Y. Ma, X. Wang, Y. Jia, X. Chen, H. Han, C. Li, Titanium dioxide-based nanomaterials for photocatalytic fuel generations, *Chem. Rev.* 114 (2014) 9987–10043, <https://doi.org/10.1021/cr500008u>.
- [5] J. Ran, J. Zhang, J. Yu, M. Jaroniec, S.Z. Qiao, Earth-abundant cocatalysts for semiconductor-based photocatalytic water splitting, *Chem. Soc. Rev.* 43 (2014) 7787–7812, <https://doi.org/10.1039/C3CS60425J>.
- [6] V.N. Rao, N.L. Reddy, M.M. Kumari, P. Ravi, M. Sathish, B. Neppolian, M.V. Shankar, Synthesis of titania wrapped cadmium sulfide nanorods for photocatalytic hydrogen generation, *Mater. Res. Bull.* 103 (2018) 122–132, <https://doi.org/10.1016/j.materresbull.2018.03.030>.
- [7] S.S. Kalanur, Y.J. Hwang, O.-S. Joo, Construction of efficient CdS-TiO<sub>2</sub> heterojunction for enhanced photocurrent, photostability, and photoelectron lifetimes, *J. Colloid Interface Sci.* 402 (2013) 94–99, <https://doi.org/10.1016/j.jcis.2013.03.049>.
- [8] S.S. Kalanur, S.H. Lee, Y.J. Hwang, O.-S. Joo, Enhanced photoanode properties of CdS nanoparticle sensitized TiO<sub>2</sub> nanotube arrays by solvothermal synthesis, *J. Photochem. Photobiol. Chem.* 259 (2013) 1–9, <https://doi.org/10.1016/j.jphotochem.2013.02.018>.
- [9] J. Chen, X.-J. Wu, L. Yin, B. Li, X. Hong, Z. Fan, B. Chen, C. Xue, H. Zhang, One-pot synthesis of CdS nanocrystals hybridized with single-layer transition-metal dichalcogenide nanosheets for efficient photocatalytic hydrogen evolution, *Angew. Chem.* 127 (n.d.) 1226–1230. doi:<https://doi.org/10.1002/ange.201410172>.
- [10] X.-J. Wu, J. Chen, C. Tan, Y. Zhu, Y. Han, H. Zhang, Controlled growth of high-density CdS and CdSe nanorod arrays on selective facets of two-dimensional semiconductor nanoplates, *Nat. Chem.* 8 (2016) 470–475, <https://doi.org/10.1038/nchem.2473>.
- [11] M. Ashokkumar, An overview on semiconductor particulate systems for photo-production of hydrogen, *Int. J. Hydrogen Energy* 23 (1998) 427–438, [https://doi.org/10.1016/S0360-3199\(97\)00103-1](https://doi.org/10.1016/S0360-3199(97)00103-1).
- [12] L.J. Zhang, T.F. Xie, D.J. Wang, S. Li, L.L. Wang, L.P. Chen, Y.C. Lu, Noble-metal-free CuS/CdS composites for photocatalytic H<sub>2</sub> evolution and its photogenerated charge transfer properties, *Int. J. Hydrogen Energy* 38 (2013) 11811–11817, <https://doi.org/10.1016/j.ijhydene.2013.06.115>.
- [13] D. Zhao, C.-F. Yang, Recent advances in the TiO<sub>2</sub>/CdS nanocomposite used for photocatalytic hydrogen production and quantum-dot-sensitized solar cells, *Renew. Sustain. Energy Rev.* 54 (2016) 1048–1059, <https://doi.org/10.1016/j.rser.2015.10.100>.
- [14] Y. Lu, X. Cheng, G. Tian, H. Zhao, L. He, J. Hu, S.-M. Wu, Y. Dong, G.-G. Chang, S. Lenaerts, S. Siffert, G. Van Tendeloo, Z.-F. Li, L.-L. Xu, X.-Y. Yang, B.-L. Su, Hierarchical CdS/m-TiO<sub>2</sub>/G ternary photocatalyst for highly active visible light-induced hydrogen production from water splitting with high stability, *Nano Energy* 47 (2018) 8–17, <https://doi.org/10.1016/j.nanoen.2018.02.021>.
- [15] X. Ning, J. Li, B. Yang, W. Zhen, Z. Li, B. Tian, G. Lu, Inhibition of photocorrosion of CdS via assembling with thin film TiO<sub>2</sub> and removing formed oxygen by artificial gill for visible light overall water splitting, *Appl. Catal. B Environ.* 212 (2017) 129–139, <https://doi.org/10.1016/j.apcatb.2017.04.074>.
- [16] J. Wang, Z. Wang, P. Qu, Q. Xu, J. Zheng, S. Jia, J. Chen, Z. Zhu, A 2D/1D TiO<sub>2</sub> nanosheet/CdS nanorods heterostructure with enhanced photocatalytic water splitting performance for H<sub>2</sub> evolution, *Int. J. Hydrogen Energy* 43 (2018) 7388–7396, <https://doi.org/10.1016/j.ijhydene.2018.02.191>.
- [17] W.S. Dos Santos, M. Rodriguez, A.S. Afonso, J.P. Mesquita, L.L. Nascimento, A.O.T. Patrocínio, A.C. Silva, L.C.A. Oliveira, J.D. Fabris, M.C. Pereira, A hole inversion layer at the BiVO<sub>4</sub>/Bi<sub>4</sub>V<sub>2</sub>O<sub>11</sub> interface produces a high tunable photovoltage for water splitting, *Sci. Rep.* 6 (2016) 31406, <https://doi.org/10.1038/srep31406>.
- [18] Z. Liu, L. Yan, High-efficiency p–n junction oxide photoelectrodes for photoelectrochemical water splitting, *Phys. Chem. Chem. Phys.* 18 (2016) 31230–31237, <https://doi.org/10.1039/C6CP06536H>.
- [19] Y.-C. Wang, C.-Y. Chang, T.-F. Yeh, Y.-L. Lee, H. Teng, Formation of internal p–n junctions in Ta<sub>3</sub>N<sub>5</sub> photoanodes for water splitting, *J. Mater. Chem. A.* 2 (2014) 20570–20577, <https://doi.org/10.1039/C4TA04501G>.
- [20] W. Wang, W. Zhang, C. Hao, F. Wu, Y. Liang, H. Shi, J. Wang, T. Zhang, Y. Hua, Enhanced photoelectrochemical activity and photocatalytic water oxidation of NiO nanoparticle-decorated SrTiO<sub>3</sub> nanocube heterostructures: Interaction, interfacial charge transfer and enhanced mechanism, *Sol. Energy Mater. Sol. Cells* 152 (2016) 1–9, <https://doi.org/10.1016/j.solmat.2016.03.016>.
- [21] J. Zhang, Q. Xu, Z. Feng, M. Li, C. Li, Importance of the relationship between surface phases and photocatalytic activity of TiO<sub>2</sub>, *Angew. Chem.* 120 (2008) 1790–1793, <https://doi.org/10.1002/ange.200704788>.
- [22] M. Zirak, M. Zhao, O. Moradlou, M. Samadi, N. Sarikhani, Q. Wang, H.-L. Zhang, A.Z. Moshfegh, Controlled engineering of WS<sub>2</sub> nanosheets–CdS nanoparticle heterojunction with enhanced photoelectrochemical activity, *Sol. Energy Mater. Sol. Cells* 141 (2015) 260–269, <https://doi.org/10.1016/j.solmat.2015.05.051>.
- [23] Y. Lin, Y. Xu, M.T. Mayer, Z.I. Simpson, G. McMahon, S. Zhou, D. Wang, Growth of p-type hematite by atomic layer deposition and its utilization for improved solar water splitting, *J. Am. Chem. Soc.* 134 (2012) 5508–5511, <https://doi.org/10.1021/ja300319g>.
- [24] I.-M. Chan, T.-Y. Hsu, F.C. Hong, Enhanced hole injections in organic light-emitting devices by depositing nickel oxide on indium tin oxide anode, *Appl. Phys. Lett.* 81 (2002) 1899–1901, <https://doi.org/10.1063/1.1505112>.
- [25] Y. Wei, X. Chang, T. Wang, C. Li, J. Gong, A low-cost NiO hole transfer layer for ohmic back contact to Cu<sub>2</sub>O for photoelectrochemical water splitting, *Small* 13 (2017) 1702007, , <https://doi.org/10.1002/smll.201702007>.
- [26] M.D. Irwin, D.B. Buchholz, A.W. Hains, R.P.H. Chang, T.J. Marks, p-Type semiconducting nickel oxide as an efficiency-enhancing anode interfacial layer in polymer bulk-heterojunction solar cells, *Proc. Natl. Acad. Sci.* 105 (2008) 2783–2787, <https://doi.org/10.1073/pnas.0711990105>.
- [27] K. Sun, F.H. Saadi, M.F. Lichterman, W.G. Hale, H.-P. Wang, X. Zhou, N.T. Plymale, S.T. Omelchenko, J.-H. He, K.M. Papadantonakis, B.S. Brunschwig, N.S. Lewis, Stable solar-driven oxidation of water by semiconducting photoanodes protected by transparent catalytic nickel oxide films, *Proc. Natl. Acad. Sci.* 112 (2015) 3612–3617, <https://doi.org/10.1073/pnas.1423034112>.
- [28] F. Malara, F. Fabbri, M. Marelli, A. Naldoni, Controlling the surface energetics and kinetics of hematite photoanodes through few atomic layers of NiOx, *ACS Catal.* 6 (2016) 3619–3628, <https://doi.org/10.1021/acscatal.6b00569>.
- [29] B. Shan, B.D. Sherman, C.M. Klug, A. Nayak, S.L. Marquard, Q. Liu, R.M. Bullock, T.J. Meyer, Modulating hole transport in multilayered photocathodes with derivatized p-Type nickel oxide and molecular assemblies for solar-driven water splitting, *J. Phys. Chem. Lett.* 8 (2017) 4374–4379, <https://doi.org/10.1021/acs.jpclett.7b01911>.
- [30] P. Wu, Z. Liu, D. Chen, M. Zhou, J. Wei, Flake-like NiO/WO<sub>3</sub> p–n heterojunction photocathode for photoelectrochemical water splitting, *Appl. Surf. Sci.* 440 (2018) 1101–1106, <https://doi.org/10.1016/j.apsusc.2018.01.292>.
- [31] B. Liu, E.S. Aydin, Growth of oriented single-crystalline rutile TiO<sub>2</sub> nanorods on transparent conducting substrates for dye-sensitized solar cells, *J. Am. Chem. Soc.* 131 (2009) 3985–3990, <https://doi.org/10.1021/ja807897z>.
- [32] C. Wang, H. Lin, Z. Xu, H. Cheng, C. Zhang, One-step hydrothermal synthesis of flowerlike MoS<sub>2</sub>/CdS heterostructures for enhanced visible-light photocatalytic activities, *RSC Adv.* 5 (2015) 15621–15626, <https://doi.org/10.1039/C4RA15632C>.
- [33] S. Rakshit, S. Ghosh, S. Chall, S. Sundar Mati, S.P. Moulik, S. Chandra Bhattacharya, Controlled synthesis of spin glass nickel oxide nanoparticles and evaluation of their potential antimicrobial activity: A cost effective and eco friendly approach, *RSC Adv.* 3 (2013) 19348–19356, <https://doi.org/10.1039/C3RA42628A>.
- [34] Y. Zhu, W. Chu, N. Wang, T. Lin, W. Yang, J. Wen, X.S. Zhao, Self-assembled NiO/RGO heterostructures for high-performance supercapacitors, *RSC Adv.* 5 (2015) 77958–77964, <https://doi.org/10.1039/C5RA14790E>.
- [35] X. Chen, L. Liu, P.Y. Yu, S.S. Mao, Increasing solar absorption for photocatalysis with black hydrogenated titanium dioxide nanocrystals, *Science.* 331 (2011) 746–750, <https://doi.org/10.1126/science.1200448>.
- [36] D. Korotin, S. Bartkowski, E. Kurmaev, M. Meumann, E. Yakushina, R. Valiev, S. Cholakh, Surface characterization of titanium implants treated in hydrofluoric acid, *J. Biomater. Nanobiotechnol.* 3 (2012) 87–91, <https://doi.org/10.4236/jbnn.2012.31011>.
- [37] H.B. Jones, Teeth and bones: application of surface science to dental materials and related biomaterials, *Surf. Sci. Rep.* 42 (2001) 75–205, [https://doi.org/10.1016/S0167-5729\(00\)00011-X](https://doi.org/10.1016/S0167-5729(00)00011-X).
- [38] C.M. Chan, S. Trigwell, T. Ouerig, Oxidation of a NiTi Alloy, *Surf. Interface Anal.* 15 (1990) 349–354, <https://doi.org/10.1002/sia.740150602>.
- [39] K.V. Khot, S.S. Mali, N.B. Pawar, R.R. Kharade, R.M. Mane, V.V. Kondalkar, P.B. Patil, P.S. Patil, C.K. Hong, J.H. Kim, J. Heo, P.N. Bhosale, Development of nanocoral-like Cd(SSe) thin films using an arrested precipitation technique and their application, *New J. Chem.* 38 (2014) 5964–5974, <https://doi.org/10.1039/C4NJ01319K>.
- [40] Y.S. Chen, J.F. Kang, B. Chen, B. Gao, L.F. Liu, X.Y. Liu, Y.Y. Wang, L. Wu, H.Y. Yu, J.Y. Wang, Q. Chen, E.G. Wang, Microscopic mechanism for unipolar resistive switching behaviour of nickel oxides, *J. Phys. Appl. Phys.* 45 (2012) 065303, , <https://doi.org/10.1088/0022-3727/45/6/065303>.
- [41] F. Meng, J. Li, S.K. Cushing, M. Zhi, N. Wu, Solar hydrogen generation by nanoscale p–n junction of p-type molybdenum disulfide/n-type nitrogen-doped reduced graphene oxide, *J. Am. Chem. Soc.* 135 (2013) 10286–10289, <https://doi.org/10.1021/ja308393w>.

1021/ja404851s.

- [42] G. Wang, H. Wang, Y. Ling, Y. Tang, X. Yang, R.C. Fitzmorris, C. Wang, J.Z. Zhang, Y. Li, Hydrogen-treated TiO<sub>2</sub> nanowire arrays for photoelectrochemical water splitting, *Nano Lett.* 11 (2011) 3026–3033, <https://doi.org/10.1021/nl201766h>.
- [43] Y. Xin, Z. Li, W. Wu, B. Fu, Z. Zhang, Pyrite FeS<sub>2</sub> sensitized TiO<sub>2</sub> nanotube photoanode for boosting near-infrared light photoelectrochemical water splitting, *ACS Sustain. Chem. Eng.* 4 (2016) 6659–6667, <https://doi.org/10.1021/acssuschemeng.6b01533>.
- [44] A. Pareek, H.G. Kim, P. Paik, P.H. Borse, Ultrathin MoS<sub>2</sub>–MoO<sub>3</sub> nanosheets functionalized CdS photoanodes for effective charge transfer in photoelectrochemical (PEC) cells, *J. Mater. Chem. A* 5 (2017) 1541–1547, <https://doi.org/10.1039/C6TA09122A>.
- [45] Y. Wang, C. Chang, T. Yeh, Y. Lee, H. Teng, Formation of internal p–n junctions in Ta<sub>3</sub>N<sub>5</sub> photoanodes for water splitting, *J. Mater. Chem. A* 2 (2014) 20570–20577, <https://doi.org/10.1039/C4TA04501G>.
- [46] W. Liu, Y. Zhang, Electrical characterization of TiO<sub>2</sub>/CH<sub>3</sub>NH<sub>3</sub>PbI<sub>3</sub> heterojunction solar cells, *J. Mater. Chem. A* 2 (2014) 10244–10249, <https://doi.org/10.1039/C4TA01219D>.
- [47] S. Martha, S. Mansingh, K.M. Parida, A. Thirumurugan, Exfoliated metal free homojunction photocatalyst prepared by a biomediated route for enhanced hydrogen evolution and Rhodamine B degradation, *Mater. Chem. Front.* 1 (2017) 1641–1653, <https://doi.org/10.1039/C7QM00055C> (Research Article).
- [48] D. Jiang, L. Chen, J. Zhu, M. Chen, W. Shi, J. Xie, Novel p–n heterojunction photocatalyst constructed by porous graphite-like C<sub>3</sub>N<sub>4</sub> and nanostructured BiOI: facile synthesis and enhanced photocatalytic activity, *Dalton Trans.* 42 (2013) 15726–15734, <https://doi.org/10.1039/C3DT52008K>.
- [49] U. Rammelt, N. Hebestreit, A. Fikus, W. Plieth, Investigation of polybithiophene/n-TiO<sub>2</sub> bilayers by electrochemical impedance spectroscopy and photoelectrochemistry, *Electrochim. Acta* 46 (2001) 2363–2371, [https://doi.org/10.1016/S0013-4686\(01\)00430-3](https://doi.org/10.1016/S0013-4686(01)00430-3).